CEAS Space J (2013) 5:57–73
DOI 10.1007/s12567-013-0047-4

ORIGINAL PAPER

# Experimental modal analysis and dynamic strain fiber Bragg gratings for structural health monitoring of composite antenna sub-reflector

**A. Panopoulou · S. Fransen ·**
**V. Gomez-Molinero · V. Kostopoulos**

Received: 12 January 2013 / Revised: 16 April 2013 / Accepted: 15 July 2013 / Published online: 29 July 2013

**Abstract** The objective of this work is to develop a new structural health monitoring system for composite aerospace structures based on dynamic response strain measurements and experimental modal analysis techniques. Fiber Bragg grating (FBG) optical sensors were used for monitoring the dynamic response of the composite structure. The structural dynamic behavior has been numerically simulated and experimentally verified by means of vibration testing. The hypothesis of all vibration tests was that actual damage in composites reduces their stiffness and produces an eigenfrequency shifting to lower values in the same sense as mass increase produces. Thus, damage was simulated by slightly varying locally the mass of the structure at different zones. The correlation between the simulated damage and the loss of stiffness was analytically defined. Experimental modal analysis based on the strain responses was conducted and the extracted strain mode shapes were the input for the damage detection expert system. A feed-forward back propagation neural network was the core of the damage detection system. The features-input to the neural network consisted of the strain mode shapes, extracted from the experimental modal analysis. Dedicated training and validation activities were carried out based on the experimental results. The system showed high reliability, confirmed by the ability of the neural network to recognize the size and the position of damage on the structure. The experiments were performed on a real structure i.e. a lightweight antenna sub-reflector, manufactured and tested at EADS CASA ESPACIO. An integrated FBG sensor network, based on the advantage of multiplexing, was mounted on the structure with optimum topology. Numerical simulation was used as a support tool at all the steps of the work. Potential applications for the proposed system are during ground qualification extensive tests of space structures and during the mission as modal analysis tool on board, being able via the FBG responses to identify a potential failure.

**Keywords** Fiber Bragg gratings · Experimental modal analysis · Composite aerospace structure · Damage detection

## 1 Introduction

Needs for structural health monitoring (SHM) in the aerospace industry are rapidly increasing due to demands to improve safety, reduce cost and inspection time while maintaining structural integrity and reliability. The performance of a spacecraft can be degraded by various factors. It is essential to have direct measurements (i.e. strain mapping, shape determination etc.), which will enable

A. Panopoulou (✉)
Structural Analysis and Verification, OHB System AG,
Universitatsallee 27-29, 28359 Bremen, Germany
e-mail: katerina.panopoulou@gmail.com

S. Fransen
European Space Research and Technology Centre
(ESA-ESTEC), Postbus 299, 2200 AG Noordwijk,
The Netherlands
e-mail: Sebastiaan.Fransen@esa.int

V. Gomez-Molinero
EADS CASA Espacio, Avenida de Aragon 404,
28922 Madrid, Spain
e-mail: Vicente.Gomez@astrium.eads.net

V. Kostopoulos
Applied Mechanics Laboratory, Department of Mechanical
Engineering and Aeronautics, University of Patras,
26500 Rio-Patras, Achaia, Greece
e-mail: kostopoulos@mech.upatras.gr

during tests and on orbit the health monitoring of the structure [1]. Fiber optic sensors are considered for potential space applications due to many advantages, i.e. lightweight, immune to electromagnetic interference, efficient multiplexing for high sensor capacity, can be embedded into structures etc. [2]. In recent works, fiber Bragg gratings (FBGs) have been utilized for modal analysis and damage detection. Paolozzi and Gasbarri [3] used fiber optic sensors for the dynamic analysis of a composite wing beam. In [4] Wu et al. demonstrated the feasibility of detecting simulated damage on an aluminium plate and debond damage on composite plates using FBGs. Huang et.al. [5] presented a damage detection system of a carbon fiber composite ð-joint structure under bending loads using FBGs. Recently, a flight test plan on a transport military aircraft was the verification of the applicability of the fiber optic Bragg grating system for airworthiness purpose [6]. The verification method was based on the comparison with the responses of conventional strain gauges technology, already used and qualified. Finally, EADS Airbus used FBGs mounted on the surface of a composite wing structure to monitor strain during loading and with change of temperature [7]. In [8] Sekine et al. studied the identification of the locations and shapes of fatigue crack in aircraft panels repaired with bonded patches using FBG sensors. The identification has been implemented by minimizing the difference between the detected and the calculated reflection spectrum of the optical sensors.

The data obtained from dynamic testing and frequency response of structures need further processing and are not always easy to interpret and handle. The issue of structural damage detection and evaluation has very recently begun to be regarded also as a pattern recognition problem. The separation and clustering of the data corresponding to their damage state and/or location has utilized artificial neural network (ANN) techniques with relative success in the majority of the works [9, 10]. Alternative pattern recognition technique is support vector machines (SVMs), introduced by Vapnik [11]. This method is utilized to organize a number of observations with respect to their corresponding labels. In general, ANNs offer solutions to three different problems: auto-association (reconstruction of a signal from noisy or incomplete data), regression/hetero-association (input–output mapping, i.e. for a given input produce an output characteristic) and classification (assign input data to given classes). Auto-association and regression are often associated with modeling application. The high levels of damage identification are based on the classification function of the ANN [12]. In future study, the comparative results between SVMs and ANN will be presented.

The basic idea is to train a neural network to recognize the behavior of the undamaged structure as well as its behavior under various damage states. When the trained network receives any data from the dynamic response of the structure it should be able to associate it to a specific damage (or non-damage) state.

In previous study, the damage detection system was developed based on statistical features in the time domain, frequency domain and in the combined time–frequency domain via the wavelet transform [13, 14]. In this study, experimental modal analysis based on the strain responses is conducted and the strain mode shapes are extracted. Strain frequency response function data were acquired from the FBGs, which were used for the experimental modal analysis. The strain mode shapes comprise the new features-input to the neural network scheme. Comparison between the efficiency of the two methods is implemented at the end of the paper.

The analysis was conducted for an antenna sub-reflector, manufactured and tested in EADS CASA ESPACIO. Damage was simulated by slightly varying locally the mass of the structure at different zones. The sub-reflector is equipped with forty strain FBG sensors for the strain mapping and one accelerometer as reference sensor. Comparison between the strain mode shapes based on analytical and experimental results is also implemented via modal assurance criterion (MAC) calculation [15]. The MAC is also calculated for the comparison of the strain mode shapes between the undamaged state and several damage states. Finally, the correlation between the simulated damage and the loss of stiffness was analytically defined. To this direction, an inverse approach was followed, i.e. instead of adding a known mass and calculate the shift of natural frequencies, the element properties (of the same area on the structure) were degraded to define at the end the reduced stiffness matrix, which causes the same frequency shift.

Potential applications for the proposed system based on experimental strain modal analysis are initially during ground qualification extensive tests of space structures and later during the mission as modal analysis tool on board. This approach will allow the correlation between the measured ground tests results of aerospace structural components and their actual performance, durability and health in space. The final objective is to use this experimental modal analysis tool on board, being able via the FBG responses to detect and localize a potential failure.

## 2 Methodology for experimental modal analysis

The frequency response function (FRF) is defined as the ratio of the response of a system $x$ ($\Omega$) (displacement, velocity or acceleration) to its excitation force $F$ ($\Omega$) [16]. The FRF is given by:

$$H(\omega) = \frac{x(\omega)}{F(\omega)} = \sum_{i=1}^{N} \psi_i \frac{1}{\omega_i^2 - \Omega^2 + i2\zeta_i\omega_i} \frac{\psi_i^T}{m_i} \qquad (1)$$

Thus, the FRF for the kth node (degree of freedom) with a single excitation force at jth DOF can be computed by Eq. 2. Frequency Response analysis computes structural response to steady-state oscillatory excitation.

$$H_k(\Omega) = \sum_{i=1}^{N} \frac{\psi_{ik}\psi_{ij}}{m_i(\omega_i^2 - \Omega^2 + i2\zeta_i\omega_i)} \tag{2}$$

where

$$\omega_i = \sqrt{\frac{k_i}{m_i}} \tag{3}$$

$\Psi$ modal matrix, $m_i$ modal mass, $\omega_i$ eigenfrequencies, $\Omega$ driving frequency, $\zeta_i$ modal damping ratio, $k_i$ modal stiffness.

Analytical calculation of the frequency response function was implemented. Excitation in this analysis is explicitly defined in the frequency domain and the results include grid point displacements, grid point accelerations and element strains, which can be directly plotted as a function of frequency. In that way, the strain frequency response functions (SFRF) are calculated [17]. The signal applied to the exciter is a sinusoid sweep with fixed amplitude. Nodes of the three interface points were connected to a point below the plate using rigid body elements, where the force and constraints are applied (Fig. 1). A large concentrated mass of $10^8$ times the sub-reflector mass was attached to the node, constrained in all rotational degrees of freedom and in two translation directions (only translation in $Z$ direction is not fixed, since refers to the direction of force generated by the shaker).

Experimentally, all strain responses, obtained from fiber Bragg grating measurements, were imported to structural dynamics toolbox (SDT, [18]) for experimental modal analysis. A wire frame model of the test structure is generated to visualize (view and animate) the test shapes. The wire frame model maps the geometry of the test structure and encompasses all test node locations. Sensor positions are defined at node locations as well as boundary conditions. The nodes correspond to all the locations where the strain optical sensor is positioned along with a number of additional nodes which aid visualization. The wireframe lines are not required but improve greatly the visualization and interpretation of the animated modes. All nodes are declared and a DOF vector is defined, which allows the description of translation DOFs in global directions.

After all measurements were imported to SDT, the SFRFs of the sensors are generated. Next step is the experimental modal identification, which is the process of estimating a parametric model (poles and mode-shapes) that accurately represents measured data. There are several methods to extract this data. In SDT, the preferred method, is the gradual building of the model using sequential peak pickings, followed by refinement (other methods include the stochastic subspace identification and the polyreference LSCE [19]). The peak picking method is widely used and the main advantage is the fast computational time. The main algorithm proposed in SDT is a frequency domain output error method that builds a model in the pole-residue form through a tuning strategy [18]. Poles are identified and consequently the strain mode shapes.

The main steps pursued were the following: finding initial pole estimates, estimating residues and residual terms for a given set of poles and optimizing poles (and residues) of the current model. After identification procedure, the visualization of the mode shapes has been implemented. The deformations were linked with the wire frame model to produce the animated plots for all damage states.

## 2.1 Test article, sensor location and experimental procedure

The item under test is a composite honeycomb antenna sub-reflector. The diameter equals to 0.9 m, the thickness is 16.62 mm and the total mass is equal to 1.5 kg. The thickness of the CFRP top and bottom face is 0.31 mm. The sub-reflector is equipped with three blades that supports the dish (two fasteners per blade). Figure 2a presents a schematic overview of the test article. Figure 2b shows the antenna sub-reflector with the FBGs mounted on it.

As mentioned above, a FE model of the structure has been developed to simulate the dynamic behaviur of the structure (Fig. 1). The honeycomb plate has been modelled in MSC/Patran and the analysis was performed with MSC/NASTRAN finite element analysis software.

To find the optimized sensor placement, since FBGs measure strain components, the strains of various elements

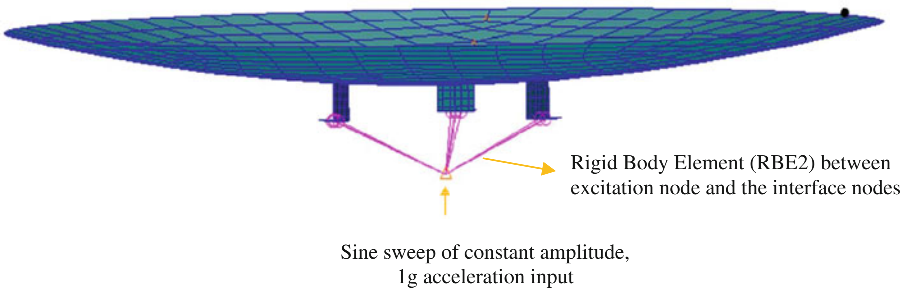

**Fig. 1** Application of sine sweep at the excitation node of the antenna sub-reflector

were calculated. A cylindrical coordinate system was created at the central node of the sub-reflector to extract the strain in tangential and circumferential direction. In addition, at each of the interface points a local coordinate system is defined with the *Z*-axis (out of plane) parallel to the reference *Z*-axis and with the *X*-axis in the radial (tangential) direction. The strain of Ply 1 (where the sensors were mounted) was extracted in both directions in the selected nodes for the first four modes (modes in FEM selected based on effective mass calculations). Based on the finite element analysis results, in the majority of the eigenmodes, the strain has higher values in the tangential/radial direction. For that reason, more strain sensors have to be mounted in this direction and less in the circumferential.

Based on the maximum strain field for the first four modes in selected elements, the sensor topology, orientation and number were defined. The optimum sensor topology, which includes 40 FBGs, is presented in Fig. 3. In total, 32 FBGs are placed in the tangential direction and 8 FBGs in the circumferential (Fig. 3).

The sub-reflector was mounted on a 489 N electrodynamic shaker (Ling V450) via the three blades (Fig. 3). The vibrator has been employed to excite the structure (*Z*-axis—out of plane—Fig. 4) with sine sweep excitation in the frequency range of interest (20–500 Hz) at 1 g level (2 octaves/min). Tests at 0.5 g, were also conducted often to verify the experimental setup. Initially, series of tests on the undamaged structure took place and the agreement between the fiber Bragg gratings results and those of the accelerometer was verified. The same results were obtained with the same test configuration at 1 g level with 1 octave/min. As a second step, the sub-reflector was 'divided' into four equal areas, on which minimum detectable lumped masses were attached to simulate damage. Initially a

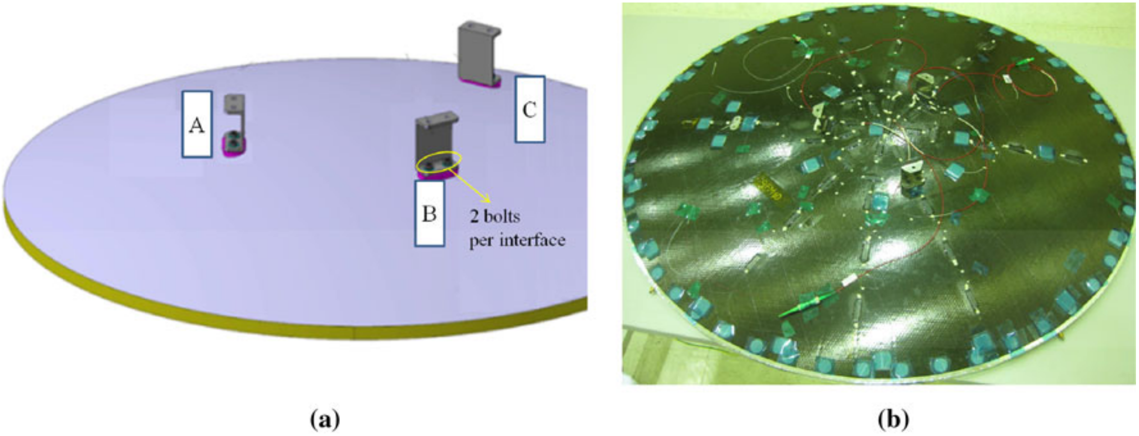

**Fig. 2** **a** Schematic overview of the test article. **b** Antenna sub-reflector with FBGs surface mounted

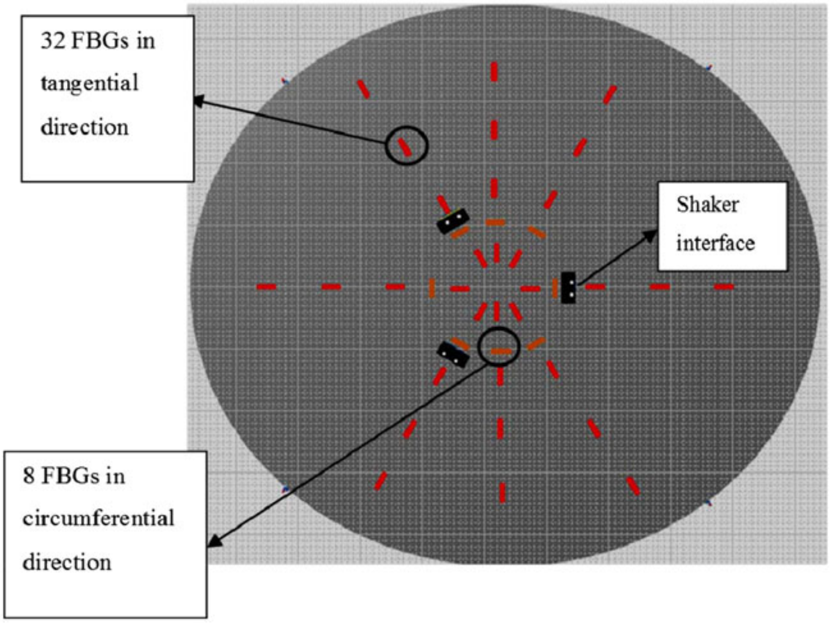

**Fig. 3** Sensor topology on the antenna sub-reflector

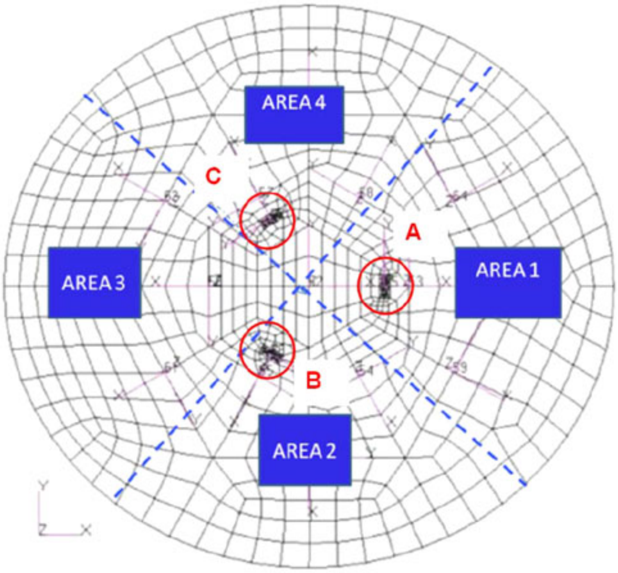

**Fig. 4** Antenna sub-reflector—damage areas (*1*–*4*) and shaker interface points (*A*-*B*-*C*)

**Table 1** Damage cases

| | Damage case | Size (g) | Location |
|---|---|---|---|
| 1 | Pristine state | – | – |
| 2 | Added mass | 27 | 1 |
| 3 | Added mass | 27 | 2 |
| 4 | Added mass | 27 | 3 |
| 5 | Added mass | 27 | 4 |
| 6 | Added mass | 49 | 1 |
| 7 | Added mass | 49 | 2 |
| 8 | Added mass | 49 | 3 |
| 9 | Added mass | 49 | 4 |
| 10 | Remove bolt | – | A |
| 11 | Remove bolt | – | B |

mass-1 = 27 g, (after calculations in FEM) was added (Fig. 4). Series of experiments with the minimum mass (mass-1) were conducted. Experiments with a second lumped mass equal to 49 g (mass-2) also took place. For each 'damage state', 30 repetitions were made at 1 g vibration amplitude level. A large data set of recorded strain responses from the FBG sensors was obtained for each damage state and damage location. As a next step, real damage was introduced to the structure by removing one fastener at the interface between the antenna sub-reflector and the shaker at two different locations (Fig. 4a, b). All damage cases are summarized in Table 1.

Taking into account the Nyquist–Shannon sampling theorem, it was concluded that the scanning rate of 1 kHz of the interrogation unit was suitable for conducting the experiments and measuring the dynamic response with FBGs for the first 4 modes. The 1 kHz high speed optical sensing interrogation unit (SM 130 Micron Optics®, 2 channels) was used during these experiments to provide the sensors with optical power as well as to receive the FBG responses [20]. The FBGs were able to measure the dynamic response up to approximately 400 Hz.

For the calculation of the SFRFs of the system, the input is obtained from the pilot accelerometer (mounted on the shaker interface plate). The output is based on the FBGs, which were located closer to the interface (high strain values). In total, the responses from 26 FBGs were taken into account for the experimental modal analysis.

## 3 Methodology for test/analysis correlation: MAC calculation

Correlation criteria are used to analyse the similarity and differences between two sets of results, which are test and analysis results in the current case. Ideally these criteria should quantify the ability of the two models to make the same predictions. The correlation between the experimental and analytical results is evaluated via MAC calculation, by comparing the mode shapes (strain mode shapes) of the two models. The MAC works independently from the individual scaling of measured and analytical mode shape vectors. Nevertheless, care should be taken such that the number of sensors allows to adequately represent the mode shapes in the entire frequency range of interest [21].

Based on the experimental strain modal analysis, which is described in the previous paragraph the SFRFs are calculated for a certain number of nodes/sensor locations. The experimental FRFs are formed based on the optical sensor responses as output and on the pilot accelerometer as input.

Next step is the topology correlation, where test and model geometrical and sensor configurations are correlated (also the coordinate system update for the test nodes if there is a coordinate system mismatch is also included). In the finite element analysis, initially the ply strain is calculated for all nodes. The strain is calculated always in the direction of the optical fiber sensor to have comparable results. To implement the sensor/node matching, the ply strains of the nodes where the sensors are located are selected and the SFRFs are extracted based on these selected locations.

The FEM results are then imported automatically in structural dynamics toolbox and the modal assurance criterion is calculated evaluating the quantitative similarity between the two models.

The methodology described above is summarized in Fig. 5. Modal assurance criterion is also calculated between the strain mode shapes of the undamaged structure and the strain mode shapes of the structure with the different states of damage.

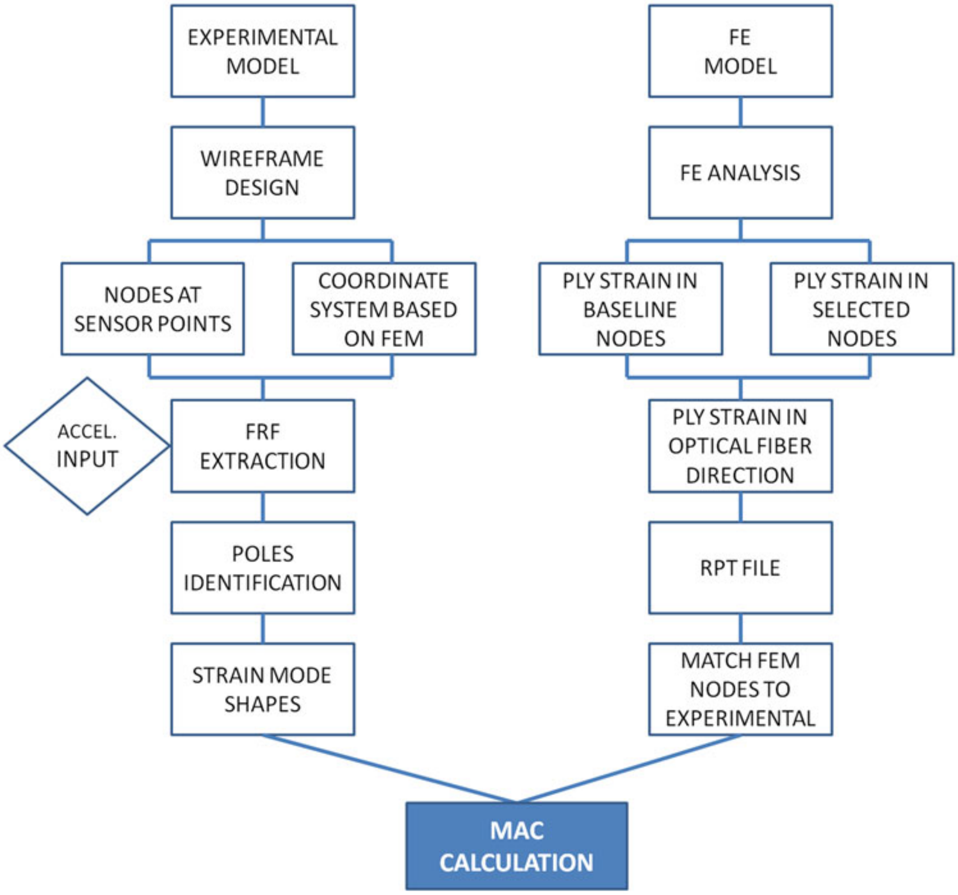

**Fig. 5** Methodology followed for MAC calculation based on experimental modal analysis using FBGs

## 4 Modal analysis for antenna sub-reflector

### 4.1 Experimental strain mode shapes extraction

Experimental modal analysis is performed for the antenna sub-reflector. Main target is to extract the strain mode shapes and to create strain mapping of the structure by overcoming the problem of spatial aliasing. The responses from the FBGs were taken into account for the experimental modal analysis.

A wire frame model of the test structure was generated to visualize the test shapes (Fig. 6). For the calculation of the SFRFs of the system the input was obtained from the pilot accelerometer, which was mounted on the interface plate between the antenna and the shaker (Fig. 7). After all measurements were imported, the SFRFs of the sensors were generated (Fig. 8). The modal model was constructed using these SFRFs. Next step was the experimental modal identification that accurately represents measured data. Poles were identified and consequently the strain mode shapes.

After identification procedure, the visualization of the mode shapes has been implemented. The deformations were linked with the wire frame model to produce the animated plots [22]. The experimental strain mode shapes as well as the analytical strain mode shapes for the first four modes are illustrated in Fig. 9.

### 4.2 Modal assurance criterion/FEM–Test: experiments

Table 2 reports a comparison between the target modes (calculated in FEM) and the modes derived experimentally. In FEM calculations, the modes were selected based on their effective mass. The table illustrates that all the correlated modes in the finite element model ($f_q$) have natural frequencies whose values do not diverge by more than 1.5 % from the corresponding experimentally derived values ($f_r$). The modal frequency discrepancy $\varepsilon_f$ is calculated by Eq. 4 [23] (Fig. 10). The mass of the sub-reflector calculated in FEM differs by less than 5 % from the actual mass ($m_{\mathrm{FEM}} = 1.57$ kg)

$$\varepsilon_f = \frac{f_r}{f_q} \times 100\ \%. \tag{4}$$

The first step for the comparison of the two models was to compare the geometry and to reduce the number of nodes of the finite element model to match the experimental model. The FEM has many more degrees of

**Fig. 6** Wireframe model combined with FEM

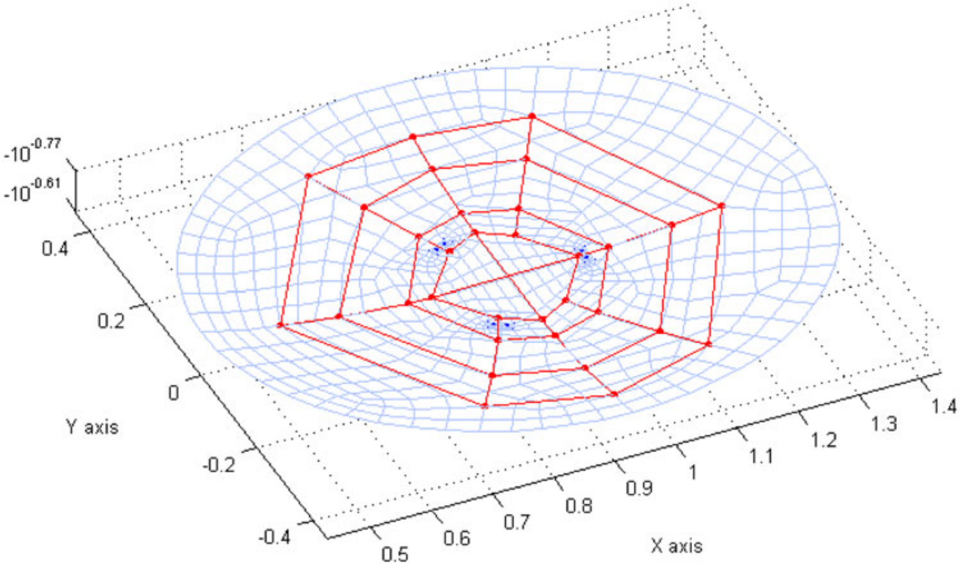

**Fig. 7** Input (pilot) accelerometer of the sub-reflector

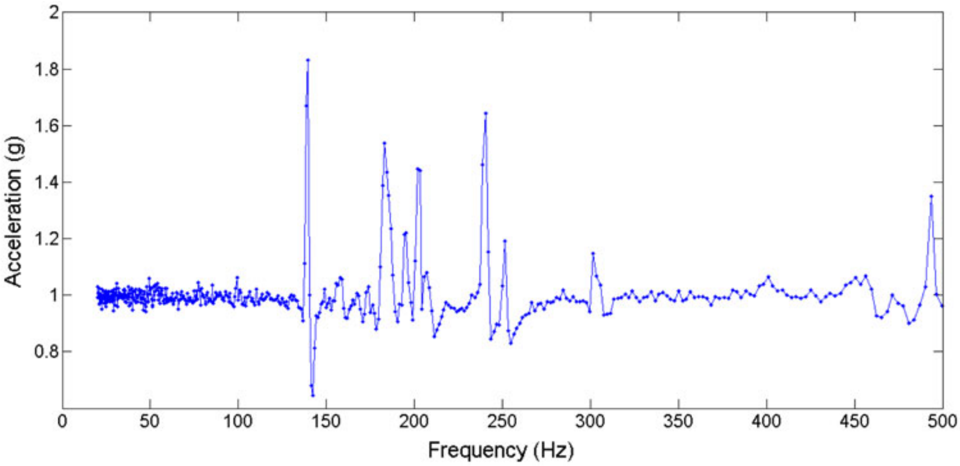

**Fig. 8** Pole estimation and optimization of the sub-reflector in SDTools

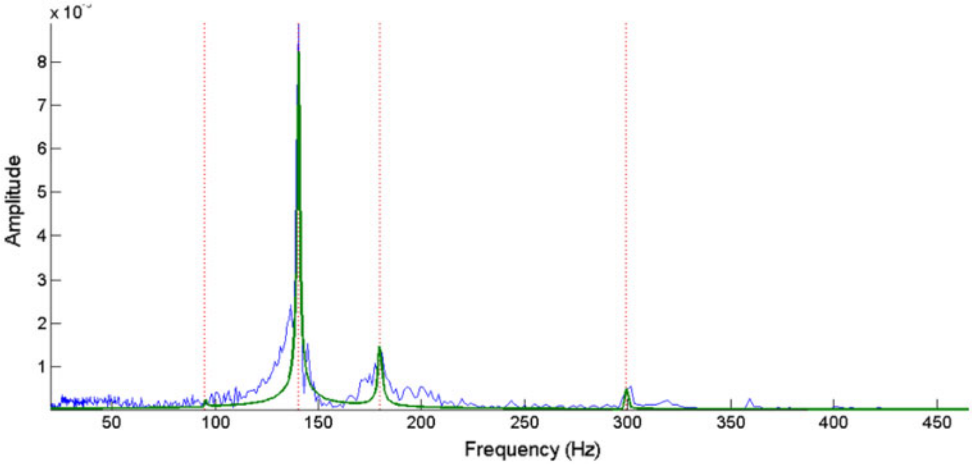

freedom than the nodes of the test structure. To compare the two models, a reduction in the FEM is necessary, where all the nodes have to correspond with the measurement points. This reduced representation or this test-analysis model (TAM) enables a quantitative comparison of the analytical model’s accuracy during post-test correlation.

**Fig. 9** Experimental and analytical strain mode shapes for the first four modes (no damage)

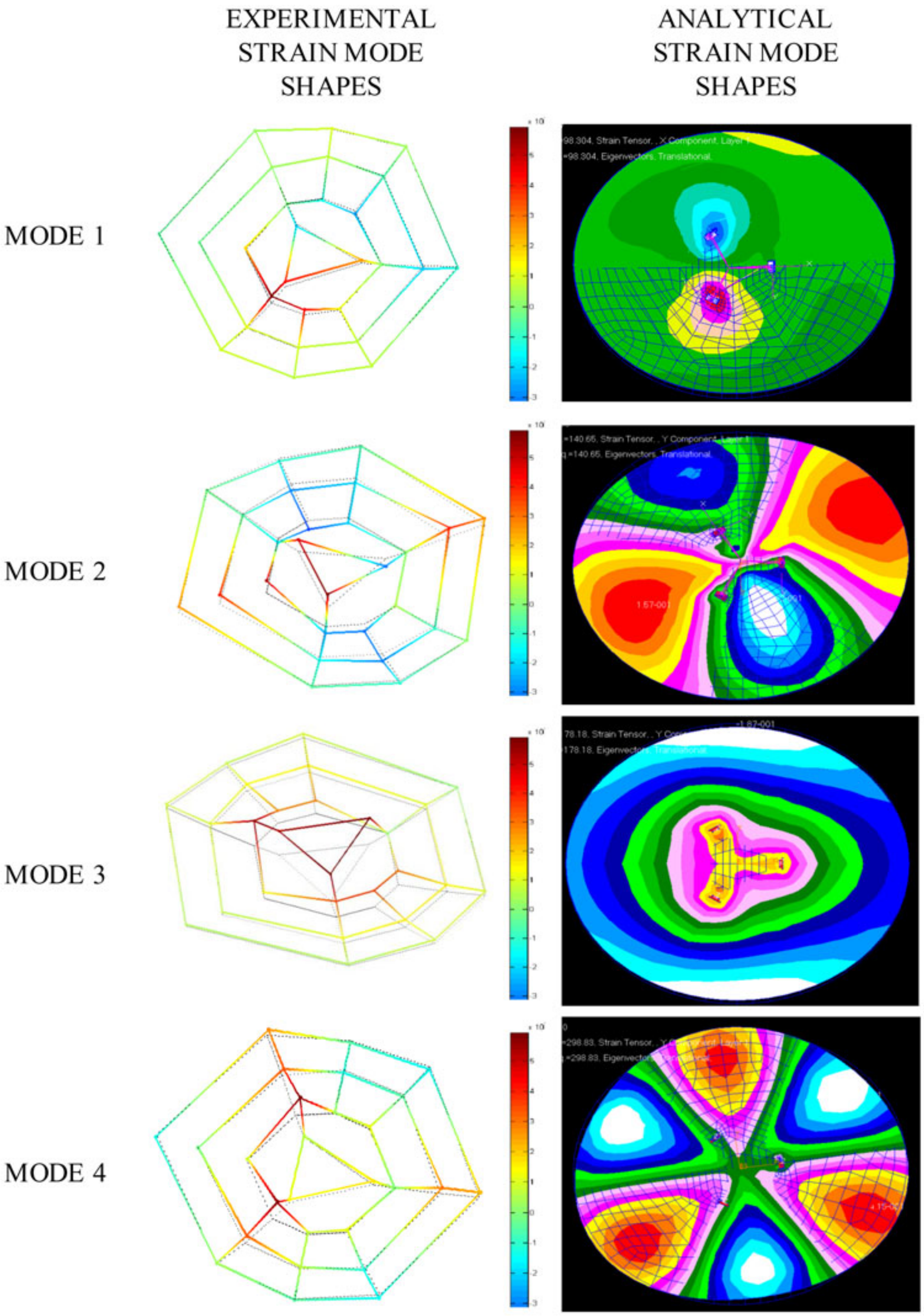

**Table 2** Experimental and analytical natural frequencies of the subreflector

| | $F_{\text{experimental}}$ | $F_{\text{FEM}}$ | $\Delta f$ (Hz) | $\varepsilon_f$ (%) |
|---|---|---|---|---|
| Mode 1 | 96.78 | 98.2 | 1.42 | 1.4 |
| Mode 2 | 141.3 | 140.65 | 0.65 | 0.3 |
| Mode 3 | 179.5 | 178.18 | 1.32 | 0.7 |
| Mode 4 | 300.1 | 298.83 | 1.27 | 0.4 |

The location of the sensor points was chosen to be coincident with the finite element grid points and the coordinate system was the same as the finite element model to simplify the modal correlation step. To calculate the strain tensor in the FEM model, the strain of Ply 1 (where the sensors were mounted) was extracted in the tangential/radial direction (which is the direction of the optical fiber) in the selected nodes. As mentioned in the methodology description, a

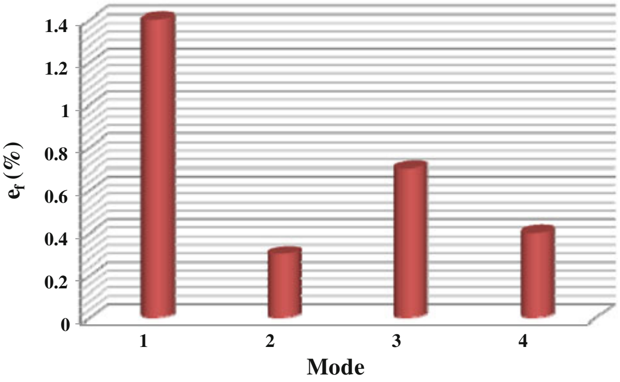

**Fig. 10** Modal frequency discrepancy (%) between the measured and analytical natural frequencies of the sub-reflector

**Table 3** MAC between experimental and FEM strain modes of the antenna sub-reflector

| MAC | FEM mode 1 | FEM mode 2 | FEM mode 3 | FEM mode 4 |
|---|---|---|---|---|
| EXP mode 1 | 0.82 | 0.007 | 0.54 | 0.14 |
| EXP mode 2 | 0.01 | 0.70 | 0.19 | 0.13 |
| EXP mode 3 | 0.47 | 0.05 | 0.90 | 0.11 |
| EXP mode 4 | 0.04 | 0.11 | 0.16 | 0.75 |

cylindrical coordinate system was created at the central node of the sub-reflector to extract the strain in tangential/radial direction. Table 3 reports the diagonal and off-diagonal term values of the MAC calculation between the correlated modes derived from FEM and the modes obtained experimentally. The results, as shown, are in good agreement with the analytical mode shapes (Figs. 11, 12, 13). In Table 3, it is noticed that the MAC values between experimental mode 1 and analytical mode 3, as well as between experimental mode 3 and analytical mode 1, are relatively high (MAC ~0.5). In Fig. 11, these modes are compared between the experimental nodes and the selected nodes of the finite element model, which correspond to the experimental nodes. Based on these nodes, there is a similarity between the strain behavior of the two models, in terms of strain concentration at the interface points, which explains the higher off-diagonal values for these two modes.

### 4.3 Modal assurance criterion/experimental damage cases

The MAC is calculated for all damage states based on the experimental results only to have a first indication of the effect of the damage size for each experimental mode at the various positions. The MAC is calculated between the experimental 'no damage' state and the various damage states. Part of the results is presented in Table 4.

As the lumped mass is attached to the structure, the strain distribution of the mode is affected. The MAC decreases gradually as the lumped mass increases since the mode shapes are affected directly. In the majority of the modes, the mode shapes are affected also according to the mass location, and the change is more significant when the lumped mass is positioned close to the areas where the strain is maximum (at modes 1, 2, 4). It is also noticeable that the third mode remains the same with the addition of the various masses at the four positions (MAC = 0.99). The third mode is the first bending mode along the *Z*-axis (drum mode) and even though the natural frequency decreases with the additional mass, the mode shape is not affected (first mode with a circular nodal line). Figure 12 illustrates the second mode shape without damage and with added mass-2 at position 4 (Fig. 3; Table 1 describe the damage areas). The MAC is very low (MAC = 0.41) since the strain mode shape has been affected importantly with the mass addition. The strain nodal lines have been rotated to almost 90°.

As mentioned above, Table 4 shows the MAC calculated based on the experimental model only between the undamaged strain mode shape for each mode and the strain mode shape after the mass addition. Based on the diagonal terms, the MAC based on strain mode shapes can identify the existence of the damage. It is expected that the MAC decreases gradually with the increase of the added mass in all modes, as described above for the second mode. Nevertheless, Table 4 shows that in some modes, the MAC is higher (between strain mode shapes without damage and strain mode shapes with damage) when the bigger mass is attached to the structure when compared to the smaller mass. For example, the MAC value for the fourth mode increases with the increase of mass.

The low sensor density on the structure in combination with the symmetry of the fourth mode in the strain mode shapes between the pristine model and the one with mass two attached to it, is a potential reason why the MAC in the experimental model between the undamaged state and the damage state with the bigger lumped mass at position 2 is higher (MAC = 0.45) when compared to the MAC between undamaged state and the smaller lumped mass at the same position. The strain mode shape is being triggered by the mass addition resulting in the rotation of this mode (as in mode 2, Fig. 12) and in low MAC result. By increasing the number of strain sensors on the antenna sub-reflector the problem of spatial aliasing could be overcome. Nevertheless, the intent of this study is to build a damage detection technique based on strain mode shapes as input parameter for the ANN and not on the calculated MAC

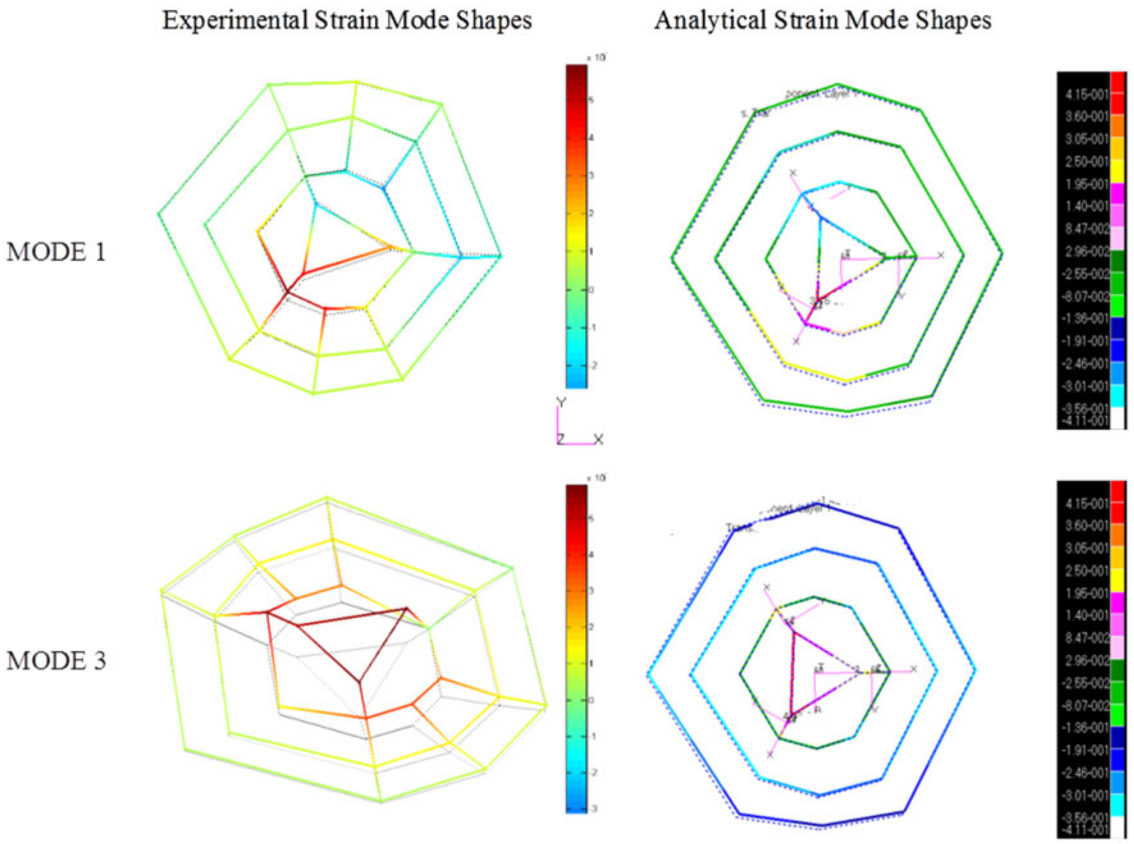

**Fig. 11** Experimental and analytical strain mode shapes (selected nodes) for the first and third mode (no damage)

values. From the changes in MAC values, it was able to detect the presence of damage, but not the location and extent of damage (global indicator).

The MAC was also calculated based only on the finite element model for the forth mode for both damage cases based only on the nodes that correspond to the sensor location. It was found that the MAC values between the undamaged state and the damage state with the smaller lumped mass at position 2 is equal to 0.33, while for the bigger mass is equal to 0.44. Hence, this difference of the MAC in this case can be validated also in FEM. At the end of Table 4, the MAC between the undamaged state and the states without bolts in the interfaces is calculated. Since the boundary conditions have an important role in the dynamic behavior of the structure, the important decrease of the MAC values in all modes is an expected result.

## 5 ANN based on experimental modal analysis

Experimental modal analysis was conducted to generate the ANN data. All the analyses are based on the FBG responses on the antenna sub-reflector. Only the sensors with the higher strain values (hence the higher signal-to-noise ratio) were input for the ANN. More specifically the strain mode shapes of the group of sensors close to the interface, where the strain is higher, were finally kept as features. Data from the same sensors were also the input for the training of the neural network based on statistical features [24].

Hence, as a first step, the strain mode shapes derived from 26 FBGs comprise the features extracted for the ANN scheme. For each FBG, the first 4 modes were taken into account for the calculations. Thirty repetitions were conducted for each damage state. In total, for each damage state, 104 variables (4 modes × 26 FBGs) were calculated. In total, nine damage scenarios (eight damage cases plus the undamaged case) are generated to evaluate the ANN performance (Table 5). As part of the pre-processing, the strain values are normalized so that the maximum positive amplitude is equal to one.

To compare the validity of the results, the normalized strain for each experimental damage state is compared with the analytical one. Figure 14 illustrates the normalized strain value for the first mode of the same node/sensor for nine damage states. The analytical model results match well with the experimental results for the maximum and minimum normalized strain values between the various damage states. In both models, the maximum strain appears

**(a)** No damage

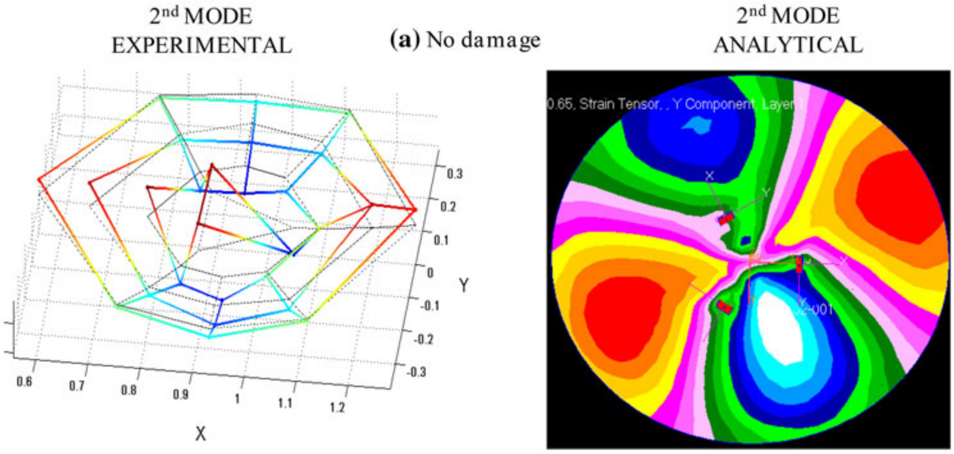

**(b)** Mass 2 Position 4

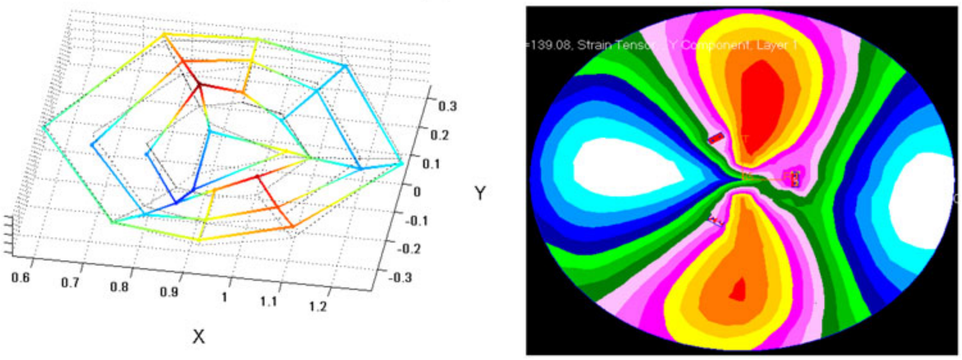

**Fig. 12** Comparison between the second strain mode at the undamaged and damage state with lumped mass no. 2 at position 4, for the experimental model (*left*) and FEM (*right*) of the antenna sub-reflector

at damage state no. 8 (Table 1, mass-2 at position 3), while the minimum strain is observed at the damage state no. 9 (Table 1, mass-2 at position 4). In addition, the strain has the second higher value in the damage state no. 3 (Table 1, mass-1 at position 2) in both models. In the other damage states, the results, between FEM and FBG output in terms of absolute normalized strain value are not in good agreement, but this difference can be, in part, attributed to small errors in the exact positioning of the FBGs and the added mass when compared to the FEM nodes for the strain extraction. Moreover, due to the concentration at the interfaces in terms of strain at the first mode, it is difficult to obtain very accurate results of strain distribution. Other factor attributed to this difference is the quality of the complete representation of the real mechanical testing conditions in the FEM model. Nevertheless, by comparing the natural frequencies of the two models, the difference is less than 1.5 %.

After obtaining the strain mode shapes, the absolute difference between the undamaged and damaged state is determined

$$\Delta(\varepsilon_i)\left|\varepsilon_{i,\text{no\_damage}}\right| - \left|\varepsilon_{i,\text{with\_damage}}\right|_{i=1:26}. \quad (5)$$

The absolute difference of the strain mode curves was calculated for all modes and damage states. This feature was also normalized by setting the largest value equal to one. The maximum difference occurs at the nodes close to the damage location for the majority of the nodes. This difference also indicates that the normalized strain mode shapes can be used as features for the ANN for the damage localization.

A multi layer perceptron with Levenberg–Marquardt (LM) back propagation algorithm is utilized to train the ANN for the detection of the simulated damage [25]. The back propagation neural network has got ten layers (i.e. input layer, output layer and ten hidden layers). The input layer neurons represent the first four relative strain mode shapes between the damage states for all sensors. Each of the nine simulated damage cases/positions corresponds to 30 observations. That is 270 observation vectors in total. For each damage state 104 variables were calculated. The number of features was reduced based on the sensor responses that show significant difference between the several damage states. Tables 5 and 6 summarize the input for the ANN scheme.

The output layer neurons represent the damage size and location. Each observation vector is assigned to a label. The label should be of an appropriate form so that the ANN will be capable of rendering some meaningful decision boundaries. Table 7 summarizes the labels assigned to each

**Fig. 13** Experimental and analytical strain mode shapes (no damage, mass 1 at position 2, and mass 2 at position 2)

4$^{th}$ mode EXPERIMENTAL 4$^{th}$ mode FEM

**(a) No damage**

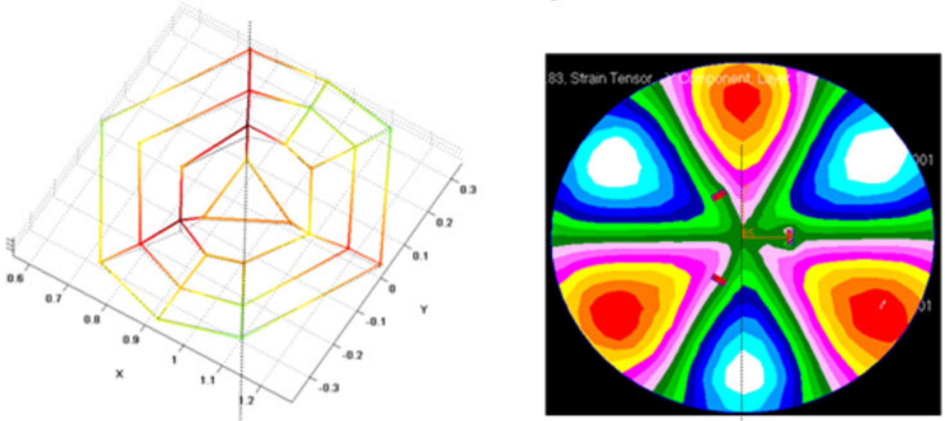

**(b) Mass No 2 Position 2**

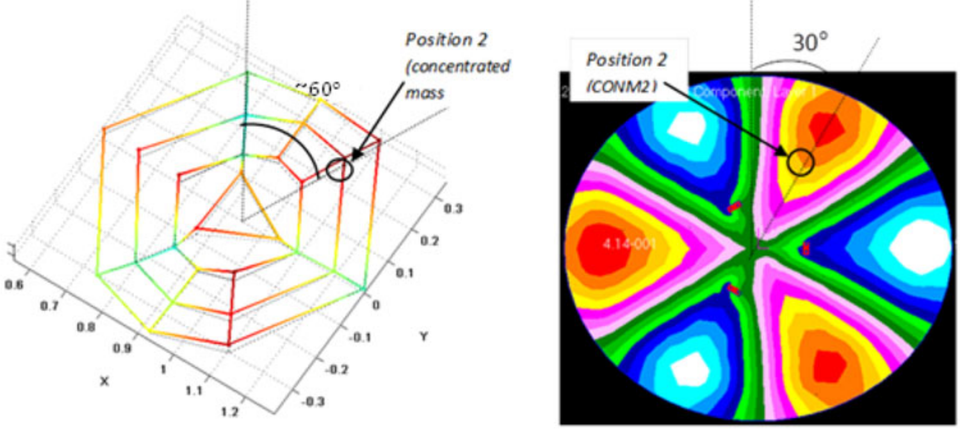

**(c) Mass No 3 Position 2**

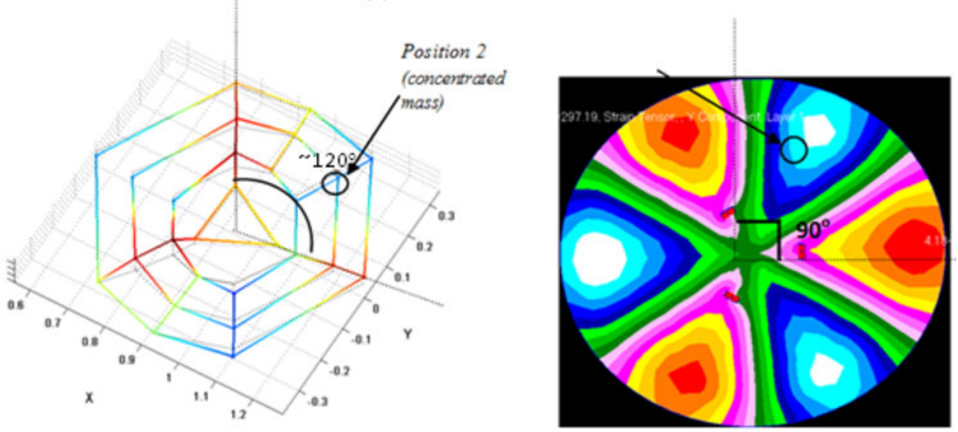

damage scenario. Tangent sigmoid transfer function is utilized for all layers [25]. All the steps for the damage detection using ANN techniques based on experimental modal analysis inputs are illustrated in Fig. 15.

As mentioned above, the optimization of ANN parameters took place through the LM algorithm. The drawback of the algorithm is that it is prone to local minima. A solution to this problem is the insertion of stochasticity to the optimization procedure. Stochasticity is inserted at the beginning of the algorithm, in the initialization of ANN parameters. The initialization algorithm (Nguyen–Widrow) chooses values to distribute the active region of each

**Table 4** MAC calculation between several damage states and undamaged state (based only on experimental strain mode shapes)

| MAC | EXP mode 1 | EXP mode 2 | EXP mode 3 | EXP mode 4 |
|---|---|---|---|---|
| Mass 1 Position 2 | | | | |
| No damage | | | | |
| EXP mode 1 | 0.94 | 0.02 | 0.41 | 0.36 |
| EXP mode 2 | 0.02 | 0.99 | 0.02 | 0.01 |
| EXP mode 3 | 0.57 | 0.03 | 0.99 | 0.82 |
| EXP mode 4 | 0.10 | 0.03 | 0.20 | 0.13 |
| Mass 2 position 2 | | | | |
| No damage | | | | |
| EXP mode 1 | 0.91 | 0.03 | 0.40 | 0.05 |
| EXP mode 2 | 0.04 | 0.84 | 0.03 | 0.05 |
| EXP mode 3 | 0.51 | 0.20 | 0.99 | 0.08 |
| EXP mode 4 | 0.06 | 0.09 | 0.19 | 0.45 |
| Mass 1 position 4 | | | | |
| No damage | | | | |
| EXP mode 1 | 0.95 | 0.05 | 0.41 | 0.16 |
| EXP mode 2 | 0.02 | 0.91 | 0.01 | 0.02 |
| EXP mode 3 | 0.38 | 0.06 | 0.99 | 0.53 |
| EXP mode 4 | 0.05 | 0.01 | 0.21 | 0.22 |
| Mass 2 position 4 | | | | |
| No damage | | | | |
| EXP mode 1 | 0.91 | 0.01 | 0.42 | 0.18 |
| EXP mode 2 | 0.08 | 0.41 | 0.02 | 0.01 |
| EXP mode 3 | 0.61 | 0.07 | 0.99 | 0.52 |
| EXP mode 4 | 0.09 | 0.02 | 0.20 | 0.26 |
| No bolt Position A | | | | |
| No damage | | | | |
| EXP mode 1 | 0.48 | 0.04 | 0.41 | 0.03 |
| EXP mode 2 | 0.03 | 0.87 | 0.01 | 0.04 |
| EXP mode 3 | 0.40 | 0.03 | 0.91 | 0.04 |
| EXP mode 4 | 0.06 | 0.02 | 0.19 | 0.62 |
| No bolt position B | | | | |
| No damage | | | | |
| EXP mode 1 | 0.38 | 0.04 | 0.42 | 0.15 |
| EXP mode 2 | 0.03 | 0.98 | 0.01 | 0.01 |
| EXP mode 3 | 0.34 | 0.02 | 0.99 | 0.51 |
| EXP mode 4 | 0.06 | 0.02 | 0.21 | 0.76 |

neuron in the layer evenly across the layer's input space [26]. Due to this stochasticity, multiple training efforts of the ANN model were necessary to obtain a trustworthy efficiency measure. For the current work, the cross-validation testing method was implemented. Cross validation is a simple method for testing classification or regression models. It is especially handy when there are relatively few observations corresponding to a particular decision class. Cross validation involves a number of tests for a particular model. This asset eliminates to a large extent the stochasticity inserted by the initialization algorithm. Cross validation was implemented as follows:

Data base comprises 9 simulated damage cases/positions, each corresponding to 30 observations. That is 270 observation vectors in total. Each group is split into three smaller sets of ten observations. For each latter set, nine observations are kept for training and one for testing (leave-one-out test) the particular ANN scheme. Therefore, for each damage case, 3 × 9 = 27 observations are kept for training and 3 for testing the ANN scheme. In total, out of 270 data vectors, 243 were kept for training of the ANN and 27 were used for testing of the resulting network. More than ten training–testing cycles take place, each with a different training–testing group. The average ANN classification efficiency is 90 % (Table 8).

So far only the strain mode shapes were utilized as inputs for the expert system. To test whether the classification efficiency can be improved with the addition of more features extracted from the experimental modal analysis, also the normalized natural frequencies ($f_i$, $i = 1{:}4$) were used as features. The classification efficiency improves to 91 % (Table 8).

## 6 Lumped mass: loss of stiffness correlation

The hypothesis of all vibration tests was that actual damage in composites reduces their stiffness and produces the same result as mass increase produces. In the experimental approach followed, instead of inducing real damage, damage was simulated with lumped masses, located at specific regions of the structure.

This results in a shift in eigen-frequencies and the corresponding amplitudes. In the finite element model, the damage case of added mass is simulated as lumped mass (CONM2), which is applied on the nodes of the structure, where the real mass was located [27]. Based on the lumped mass size, the frequency shift of each damage case was calculated. As described above, the frequency shift between the experimental natural frequencies with the added mass and the analytical ones with lumped mass at the same location is in very good agreement for all modes. The correlation between the added mass and stiffness has to be defined. An inverse approach is followed: instead of adding a known mass and calculate the shift of natural frequencies, the element properties (of the same area on the structure) are degraded in to define at the end the reduced stiffness matrix which causes the same frequency shift. A mass increase leads to a reduction of frequency. Hence, it should be equivalent to a difference in stiffness.

For the elements in the damaged zone, which are located around the node where the lumped mass was

**Table 5** Input table for ANN scheme

| | DAMAGE STATE | | | | | | | | |
|---|---|---|---|---|---|---|---|---|---|
| | No damage | Mass 1 | | | | Mass 2 | | | |
| | | Pos. 1 | Pos. 2 | Pos.3 | Pos. 4 | Pos.1 | Pos.2 | Pos.3 | Pos.4 |
| Mode 1<br>FBG 1<br>.<br>.<br>FBG 26 | | | | | 270 | observations | | | |
| Mode 2<br>FBG 1<br>.<br>.<br>FBG 26 | | | | | | | | | |
| Mode 3<br>FBG 1<br>.<br>.<br>FBG 26 | | 104 | vectors | | | | | | |
| Mode 4<br>FBG 1<br>.<br>.<br>FBG 26 | | | | | | | | | |

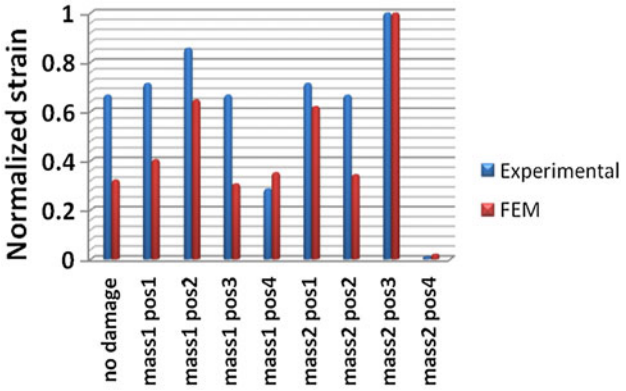

**Fig. 14** Comparison of normalized strain $\varepsilon_i$ between FEM and experimental model of the antenna sub-reflector

**Table 6** ANN Input data

| | |
|---|---|
| Observations per simulated damage scenario | 30 |
| Number of damage scenarios | 1 (no damage) + 4 (mass 1, 4 positions) + 4 (mass 2, 4 positions) = 9 |
| Total observations | 270 |

added, the properties have to be reduced to simulate the damage case. The stiffness reduction coefficient is defined as (Eq. 6):

**Table 7** Representation of simulated damage scenario for ANN training The latter representation will be applied to formulate the output vector for the training of the ANN

Output space vector representation

| Label | Label | Label | … | Label |
|---|---|---|---|---|
| damage scenario | damage scenario | damage scenario | … | damage scenario |
| 1 | 2 | 3 | … | 9 |

$$\begin{bmatrix} 1 \\ -1 \\ -1 \\ \vdots \\ \vdots \\ \vdots \\ -1 \end{bmatrix} \quad \begin{bmatrix} -1 \\ 1 \\ -1 \\ \vdots \\ \vdots \\ \vdots \\ -1 \end{bmatrix} \quad \begin{bmatrix} -1 \\ -1 \\ 1 \\ \vdots \\ \vdots \\ \vdots \\ -1 \end{bmatrix} \quad \cdots \quad \begin{bmatrix} -1 \\ -1 \\ -1 \\ \vdots \\ \vdots \\ \vdots \\ 1 \end{bmatrix}$$

$$a = \frac{G_{ij\_\text{damaged}}}{G_{ij\_\text{undamaged}}}. \tag{6}$$

Where $G_{ij\_(\text{damaged})}$ is the material equivalent property matrix for the elements in the damaged zone, $G_{ij\_(\text{undamaged})}$ is the one for the elements without damage and a the stiffness reduction coefficient.

**Fig. 15** Damage detection system based on ANN and experimental modal analysis results

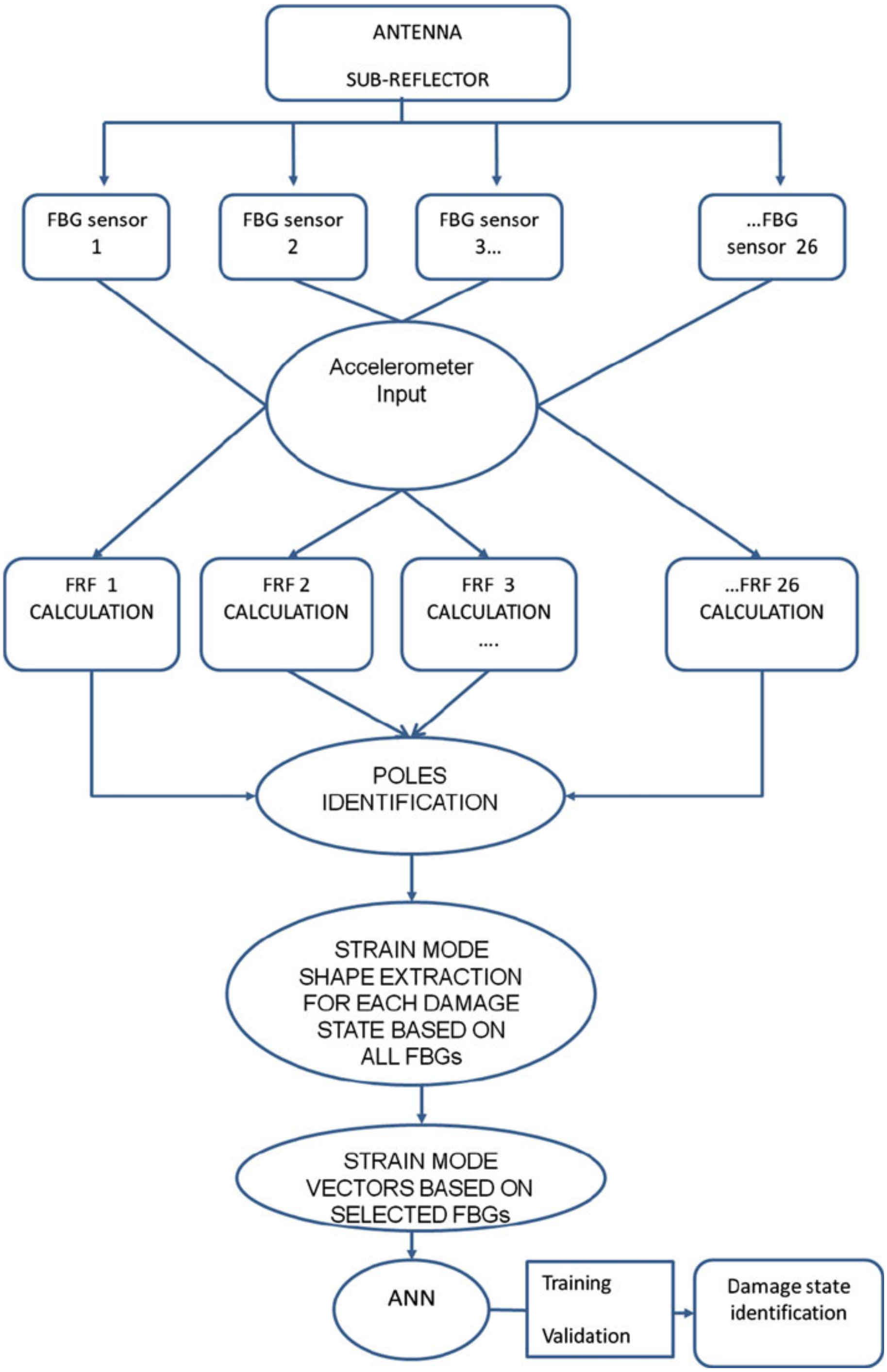

The approach that is followed is based on the conversion of PCOMP into its homogeneous equivalent shell. The transformation is performed by converting the PCOMP and MAT8 cards to PSHELL and MAT2 cards [27]. Each MAT2 card represents one of the four behaviors of the PSHELL properties (membrane property, bending, transverse shear, membrane-bending coupling). In that way the equivalent material properties that define more directly the stiffness of the shell elements can be modified. The material properties of the elements where the lumped mass was added are reduced gradually to a level that the calculated eigen-frequencies reach the values of the frequency shift that the added masses cause. The diagram of Fig. 16 summarized the modeling procedure:

The degraded material properties are obtained by multiplying the properties of MAT2 with the stiffness

**Table 8** ANN scheme and Classification Efficiency based on experimental modal analysis

| Antenna sub-reflector ANN scheme based on experimental modal analysis | |
|---|---|
| Number of hidden neurons | 10 |
| ANN optimization algorithm | Levenberg–Marquadt |
| Training examples | 243 |
| Testing examples | 27 |
| Maximum training epochs | 500 |
| Number of trainings | 10 |
| Classification efficiency (experimental strain mode shapes) | 90 % |
| Classification efficiency (experimental strain mode shapes + natural frequencies) | 91 % |
| Classification efficiency (statistical features) [24] | 89 % |

reduction coefficient. After several runs, it was concluded that the material properties related to the bending stiffness are the ones who affect more the shift in the eigen-frequencies. This was also expected since all modes are bending modes. These terms directly relate bending moment of the structure to curvature. For the case of the minimum mass ($m1 = 27$ g) the stiffness reduction coefficient for the selected elements that define the damage zone is equal to 0.65 and for the bigger mass ($m2 = 49$ g) is equal to 0.02.

## 7 Discussion: summary

This paper presented an alternative approach for damage identification based on experimental modal analysis and ANN techniques. Strain frequency response data were acquired from the optical sensors, which were used as input for the ANN. Experimental strain modal analysis was conducted for the antenna sub-reflector using structural dynamics toolbox. The analysis is implemented based on the responses of the optical sensors. As input for the SFRFs, the response from the pilot accelerometer was used and as output the FBG responses.

Modal assurance criterion was calculated between the analytical and the experimental strain mode shapes. In general, there is very good agreement between the two models (analytical and experimental) for both structures. Due to the dense topology of the sensors, a full strain mapping was done and the strain mode shapes were extracted by overcoming the obstacle of spatial aliasing.

Modal assurance criterion was also calculated between the different damage states experimentally. In the majority of the modes and damage cases, the change (decrease) of MAC was proportional to the damage size.

The ANN classification efficiency is compared between two different approaches of features extraction. In total, nine damage cases are considered as output for the ANN, which correspond to the undamaged case plus eight damage cases (two different damage sizes, four different locations).

In previous study, statistical features were extracted from the strain waveforms [24]. Statistical indices in the time domain (such as skewness, kurtosis), in the frequency domain (skewness of PSD, kurtosis of PSD) and in the combined time–frequency domain via the discrete wavelet transform (DWT), were used for feature extraction. The extracted features were indices of damage location and its extension and the classification efficiency for damage identification reached 89 % [24].

In this work, the ANN scheme is based on the experimental strain modal analysis and the extracted strain mode shapes. The strain mode shapes in combination with the calculated eigen-frequencies of the structure are the input to the neural network scheme for damage detection and classification. It was found that the neural network, with input vector based on strain mode shapes and natural frequencies reached classification efficiency equal to 91 %.

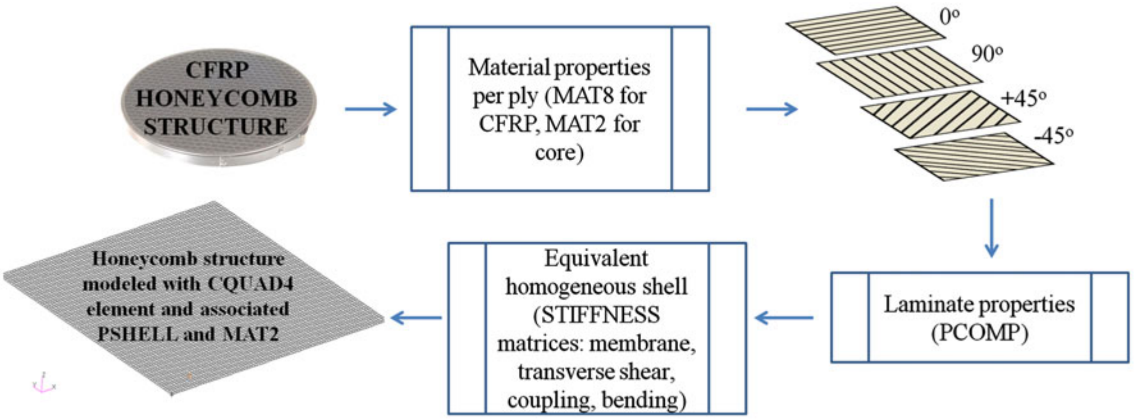

**Fig. 16** Modeling procedure

Each mode shape—feature generates decision rules for separating the various classes of test data. However, the features that play a better role in recognizing different class of damage are selected. The best features in this case are dictated by the factor of lower signal-to-noise ratio in the strain response function. More specifically, the features are extracted from sensors that are positioned close to high strain locations on the structure. The selected features can perform correct separation of the different waveforms that contribute much to the recognition of damage due to high signal-to-noise ratio. In this way, the features for the ANN are the calculated strain mode shapes and are provided a slightly simpler alternative approach for indices selection without the need of calculating and selecting features of statistical nature.

In general, the classification efficiency of the two ANN schemes based on different feature extraction procedures, i.e. on statistical features and on strain FRFs is comparable. The same sensor responses were utilized for both schemes. There is a very little difference in the classification performance of the two methods, reaching only 2 %. This proves that both methods can be potentially used for damage identification based on artificial neural network techniques. In future study, the two methods could be combined, obtaining possibly better results for damage identification.

**Acknowledgments** The authors gratefully acknowledge the support of the present work by EADS CASA Espacio and by the European Space Agency, within the frame of ESA, NPI project: methodology for innovative health monitoring of aerospace structures using dynamic response measurements and advanced signal processing. This work is part of the PhD thesis of the first of the authors.

## References

1. Friebele, E.J., Askins, S.G., Bosse, A.B., Kersey, A.D., Patrick, H.J., Pogue, W.R., Putnam, A.M., Simon, W.R., Tasker, F.A., Vincent, W.S., Vohra, S.T.: Optical fiber sensors for spacecraft applications. Smart Mater. Struct. **8**, 813–838 (1999)
2. Mckenzie, I., Karafolas, N.: Fiber optic sensing in space structures: the experience of the European Space Agency. In: Proceedings of the 17th international conference on optical fibre sensor, 5855, Bellingham (2005)
3. Paolozzi, A., Gasbarri, P.: Dynamic analysis with fibre optic sensors for structural health monitoring. In: Proceedings of meeting on multifunctional structures/integration of sensors and antennas, paper 9, RTO, France, pp. 9.1–9.24 (2006)
4. Wu, X., Ghaboussi, J., Garrett Jr, H.: Use of neural networks in detection of structural damage. Comput. Struct. **42**(4), 649–659 (1992)
5. Huang, H., Yuan, S.: Composite failure detection in ð-joint structure using fiber Bragg grating sensors. In: Proceedings of the 2nd international symposium on NDT in aerospace. Hamburg, 16 (2010)
6. Camerlingo, F.P., Cavaccini, G., Ciliberto, A., Voto., C., Iodice, M., Pezzuti, F. Alenia SHM fiber optic bragg grating (FOBG) strain sensors technology: applications and requirements. Alenia Aeronautica (2006)
7. Betz, D.C., Staudigel, L., Trutzel, M.N., Kehlenbach, M.: Structural monitoring using fiber-optic Bragg grating sensors. Struct. Health Monit. Int. J. **2**(2), 145–152 (2003)
8. Sekine, H., Fujimoto, S., Okabe, T., Takeda, N., Yokobori, T.: Structural health monitoring of cracked aircraft panels repaired with bonded patches using fiber Bragg grating sensors. Appl. Compos. Mater. **13**(2), 89–98 (2006)
9. Samanta, B., Al-Balushi, K.R.: Artificial neural network based fault diagnostics of rolling element bearings using time-domain features. Mech. Syst. Signal Process. **17**(2), 317–328 (2003)
10. Zang, C., Imregun, M.: Structural damage detection using artificial neural networks and measured FRF data reduced via principal component projection. J. Sound Vib. **242**(5), 813–827 (2001)
11. Vapnik, V.: The Nature of Statistical Learning Theory, 2nd edn. Springer, New York (1995)
12. Staszewski, W.J., Worden, K.: Signal processing for damage detection. In: Health Monitoring of Aerospace Structures: Smart Sensor Technologies and Signal Processing. Wiley, West Sussex (2004)
13. Panopoulou, A., Loutas, T., Roulias, D., Fransen, S., Kostopoulos, V.: Dynamic fiber Bragg gratings based health monitoring system of composite aerospace structures. Acta Astronaut. **7–8**(69), 445–457 (2011)
14. Panopoulou, A., Roulias, D., Loutas, T.H, Kostopoulos, V.: Health monitoring of aerospace structures using fibre Bragg gratings combined with advanced signal processing and pattern recognition techniques. Strain Int. J. Exp. Mech., fist published online: 11 Aug (2011). doi:10.1111/j.1475-1305.2011.00820.x
15. Friswell, M.I., Mottershead, J.E.: Finite Element Model Updating in Structural Dynamics. Kluwer Academic Publishers, Dordreecht (1995)
16. He, J., Fu, Z.: Modal Analysis. Butterworth-Heinemann, Oxford (2001)
17. Yam, L., Leung, T.P.: Theoretical and experimental study on modal strain analysis. J. Sound Vib. **191**(2), 251–260 (1996)
18. Balmes, E.: Structural Dynamics Toolbox User's Guide (2005)
19. Andersen, P., Brincker, R., Peeters, B., Roeck, G., Hermans, L., Krämer, C.: Comparison of system identification methods using ambient bridge test Dat. In: Proceedings of the 17 international modal analysis conference, Society of Experimental Mechanics, vol. **3**, pp. 1035–1041, Florida (1999)
20. Micron Optics.: Sensing Instrumentation and Software ENLIGHT. User guide revision 1.1018, Atlanta, United States (2008)
21. Balageas, D., Fritzen, C.P., Guemes, A.: Structural Health Monitoring. ISTE Ltd., United States (2006)
22. Bianchi, J.P., Balmes, E.: Structural Dynamics Toolbox Primer. Revised for SDT 6.2 (2010)
23. Rades, M.: Mechanical Vibrations II—Structural Dynamic Modeling. Printech, Bucharest (2010)
24. Panopoulou, A., Loutas, T., Gomez, V.M., Fransen, S., Kostopoulos, V.: Damage detection in composite sub-reflector antenna based on fibre optic sensor technology. In: Proceedings of the CD-ROM at SETEC 11 on advanced composites, the integrated system, Leiden (2011)
25. Gurney, K.: An Introduction to Neural Networks. UCL Press, London (1997)
26. Nguyen, D., Widrow, B.: Improving the learning speed of 2-layer neural networks by choosing initial values of the adaptive weights. Proc Int Joint Conf Neural Netw **3**, 21–26 (1990)
27. MSC Nastran.: Quick Reference Guide. MSC Software Corporation (2004)